buildings

MDPI

Article

Finite Element Analysis of T-Shaped Concrete-Filled Steel Tubular Short Columns with Stiffening Ribs Under Axial Compression

Xiaosan Yin [1,2], Hongliang Yue [1], Yuzhou Sun [1,2,*], Guoyang Fu [3], Jimin Li [1] and Md. Mashiur Rahman [1]

[1] School of Intelligent Construction and Civil Engineering, Zhongyuan University of Technology, Zhengzhou 450007, China; 6269@zut.edu.com (X.Y.); yuehongliang@zut.edu.cn (H.Y.); 2022109390@zut.edu.cn (J.L.); mramoshi255@outlook.com (M.M.R.)
[2] Henan Mechanics and Structures Engineering Research Center, Zhengzhou 451191, China
[3] Faculty of Science and Engineering, Southern Cross University, Gold Coast, QLD 4225, Australia; guoyang.fu@scu.edu.au
* Correspondence: sunyz@zut.edu.com

Abstract: A new type of stiffening rib is proposed to improve the mechanical performance of T-shaped concrete-filled steel tubular (CFST) columns. A finite element model was established using the general-purpose commercial software ABAQUS 2022. After verification through comparison with experimental data, the developed finite element model was employed to numerically evaluate the performance of T-shaped CFST short columns with stiffening ribs under axial compression. The results indicated that the new stiffening ribs are capable of significantly reducing the buckling deformation of the steel tube, enhancing the confinement effect of the steel tube on the core concrete, and improving the combined performance of the steel tube and the concrete. The thickness and material strength of the stiffening ribs had a notable impact on the ultimate bearing capacity and ductility of the short column specimens. When the thickness of the stiffening ribs increased from 5 mm to 8 mm, the ultimate bearing capacity correspondingly increased by 10.51% to 31.77%, while the ductility coefficient improved by 6.48% to 17.20%. When the steel strength increased from 262.50 MPa to 345 MPa and 390 MPa, the ultimate bearing capacity correspondingly increased by 17.36%, 19.78%, and 30.50%, and the ductility coefficient improved by 12%, 13.87% and 23.92%. The changes in the specifications and arrangement of the stiffening ribs had no significant effect on the ultimate bearing capacity and ductility of the specimens. The change in angle steel specifications caused variations in ultimate bearing capacity within ±5% and variations in the ductility coefficient within ±10%. Changes in the arrangement caused variations in ultimate bearing capacity within ±1% and variations in the ductility coefficient within ±5%.

Keywords: T-shaped concrete-filled steel tubular columns; short columns; stiffening ribs; finite element analysis; axial compression

check for updates

Academic Editors: You-Fu Yang and Daxu Zhang

Received: 28 November 2024
Revised: 28 December 2024
Accepted: 29 December 2024
Published: 31 December 2024

Citation: Yin, X.; Yue, H.; Sun, Y.; Fu, G.; Li, J.; Rahman, M.M. Finite Element Analysis of T-Shaped Concrete-Filled Steel Tubular Short Columns with Stiffening Ribs Under Axial Compression. *Buildings* **2025**, *15*, 112. https://doi.org/10.3390/buildings15010112

Copyright: © 2024 by the authors. Licensee MDPI, Basel, Switzerland. This article is an open access article distributed under the terms and conditions of the Creative Commons Attribution (CC BY) license (https://creativecommons.org/licenses/by/4.0/).

1. Introduction

Concrete-filled steel tubular (CFST) structures not only have the advantages of high load-bearing capacity, good ductility, light weight, and excellent seismic performance but also offer convenient construction and good economic benefits [1,2]. Thus, they have been widely used in engineering projects [3,4]. Traditional CFST columns typically use circular or rectangular cross-sections, which protrude from the wall. Thus, they take up a significant amount of indoor space and make it difficult to position furniture [5]. Designing

CFST columns to have the same thickness as the wall avoids the exposure of column corners inside the room, meets people's spatial usage requirements, and significantly improves the utilization rate of indoor space. This effectively leverages the high load-bearing capacity, good deformation performance, and fast construction speed of CFST structures. Non-standard cross-section CFST columns include L-shaped, T-shaped, and cruciform-shaped forms, with T-shaped sections being the most commonly used. However, the constraint effect of the steel tube on the core concrete in T-shaped CFST columns is mainly concentrated at the convex corners. Under an axial compression load, the steel tube at the concave corners is prone to local buckling. This may lead to separation of the steel tube from the concrete, which will reduce the overall load-bearing capacity of the component [6–8].

To improve the restraint effect at the concave corners of T-shaped CFST columns, researchers have adopted measures such as modifying the cross-sectional shape, adding restraint tie rods, and stiffening ribs. The modifications to the cross-sectional shape primarily fall into two categories [9–14]: (1) assembling several rectangular steel tubes into a T-shaped section, such as welding three rectangular steel tubes or four square steel tubes together; (2) combining rectangular steel tubes with U-shaped steel to form a T-shaped section, such as welding longitudinal rectangular steel tubes with U-shaped steel, welding transverse rectangular steel tubes with U-shaped steel, or welding longitudinal rectangular steel tubes with U-shaped steel after adding transverse steel plates inside the rectangular tubes. Additionally, T-shaped CFST columns can be formed by connecting individual rectangular CFST columns using gusset plates. The main connection methods are a single-hole gusset plate connection and a double-row gusset plate connection [15,16].

When modifying the cross-sectional form, the amount of steel used increases significantly, and the construction process becomes noticeably more complex. Therefore, methods that are structurally simple and easy to construct, such as those involving constrained tie rods and stiffening ribs, have received widespread attention in recent years [17]. Adding constrained tie rods to T-shaped steel tubes can enhance the confinement effect of the steel tube on the core concrete, increase the ultimate bearing capacity, delay local buckling of the steel tube, change the failure mode of the steel tube, and improve ductility [17–19]. By incorporating L-shaped stiffening ribs, semi-penetrating stiffening ribs, fully penetrating stiffening ribs, inclined honeycomb stiffening ribs, and built-in steel bones in T-shaped steel tube concrete columns, the axial compression stiffness, axial compression bearing capacity, and flexural bearing capacity of the T-shaped steel tube concrete columns are improved, and their seismic performance is enhanced [20–25].

To improve the mechanical performance of T-shaped CFST columns and promote the widespread use of T-shaped CFST structures, this paper proposes a new type of stiffening rib. Specifically, angle steel of the same height as the component was installed at the midpoint of the wide side and the concave corners of the T-shaped CFST column. Compared to measures that modify the cross-sectional form, this new type of stiffening rib significantly reduced the amount of steel used and greatly enhances the convenience of construction. To understand the impact of the new stiffening ribs on the mechanical performance of T-shaped CFST columns, a finite element model using ABAQUS software was employed. After validation through comparisons with experimental data, the effects of key parameters such as the thickness, specifications, strength, and arrangement of the stiffening ribs on the bearing capacity and load–longitudinal displacement relationships of the new stiffening rib T-shaped CFST columns were analyzed.

2. Finite Element Modeling of T-Shaped Concrete-Filled Steel Tubular Short Columns

Constitutive Models

In the finite element model, the core concrete of T-shaped CFST short columns uses a plastic damage model, the Concrete-Damaged Plasticity (CDP) model. This model can better simulate the tensile and compressive properties of concrete; the relevant parameters are summarized in Table 1.

Table 1. Parameters used in the concrete-damaged plasticity model.

Expansion Angle ψ/(°)	Eccentricity Ratio m	f_{b0}/f_{c0}	K	Viscous Parameter μ_v
30	0.1	1.16	0.6667	0.0005

Note: f_{b0}/f_{c0} is the ratio of biaxial to uniaxial compressive strength; K is the ratio of the second stress invariant on the tensile meridian to that on the compressive meridian.

The constitutive model of concrete adopts the stress–strain relationship related to the equivalent confinement coefficient [26]. The expression for the compression stage is as follows:

$$y = \begin{cases} 2x - x^2 & x \le 1 \\ \frac{x}{\beta_0 \cdot (x-1)^{\eta} + x} & x > 1 \end{cases}, \quad (1)$$

where $x = \frac{\varepsilon}{\varepsilon_0}, y = \frac{\sigma}{\sigma_0}, \sigma_0 = f_c$, ε_0 is the strain corresponding to the peak compressive stress, $\varepsilon_0 = \varepsilon_c + 800 \cdot \xi^{0.2} \cdot 10^{-6}$, $\varepsilon_c = (1300 + 12.5 \cdot f_c) \cdot 10^{-6}$, σ_0 is the peak compressive stress, and ε_0 is the compressive strength of the concrete cylinder.

The expression of the parameter β_0 is as follows:

$$\beta_0 = \begin{cases} \left(2.36 \times 10^{-5}\right)^{[0.25 + (\xi - 0.5)^7]} \cdot f_c^{0.5} \cdot 0.5 & (\xi \le 3.0) \\ \frac{f_c^{0.1}}{1.2\sqrt{1+\xi}} & (\xi > 3.0) \end{cases}, \quad (2)$$

where ξ is the constraint effect coefficient, $\xi = \frac{A_s f_y}{A_c f_{ck}}$; f_y and f_{ck} are the yield strength of steel and the axial compressive strength of concrete, respectively; and A_s and A_c are the cross-sectional areas of the steel tube and the concrete, respectively.

The expression for the influence coefficient of the sectional aspect ratio η is as follows:

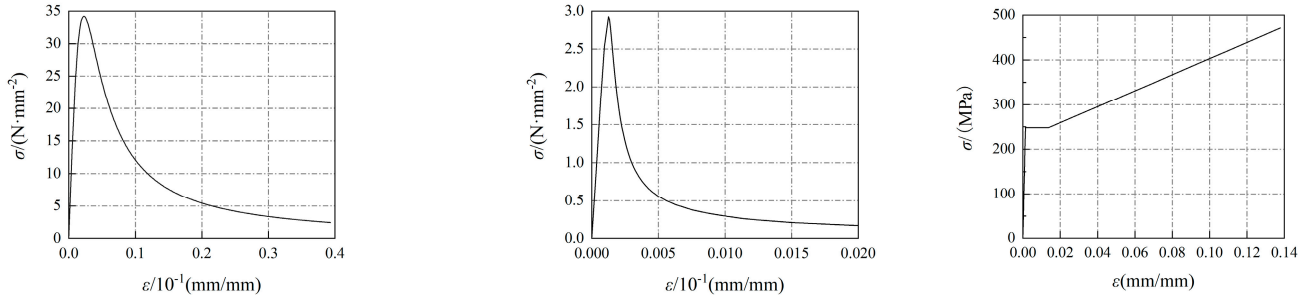
$$\eta = \begin{cases} 2 \\ 1.6 + 1.5/x \end{cases}. \quad (3)$$

The expression for the tension stage is as follows:

$$y = \begin{cases} 1.2x - 0.2x^6 & x \le 1 \\ \frac{x}{\alpha_t \cdot (x-1)^{1.7} + x} & x > 1 \end{cases}, \quad (4)$$

where $x = \frac{\varepsilon}{\varepsilon_p}$, ε_p is the peak strain corresponding to the peak tensile stress of the concrete, $y = \frac{\sigma}{\sigma_p}$, σ_p is the peak tensile stress of the concrete, $\alpha_t = 0.312 f_t^2$, and f_t is the uniaxial tensile strength of the concrete.

The elastic modulus of the concrete is taken as $E_c = 4730\sqrt{f_{cu}}$, the cube compressive strength f_{cu} is 38.22 MPa, and the Poisson's ratio μ_c is 0.2. Substituting Equation (1) into Equation (4), the stress–strain curves of the concrete are obtained as shown in Figure 1a,b.



(**a**) Concrete under compression (**b**) Concrete under tension (**c**) Steel

Figure 1. Stress–strain curves of concrete and steel.

In the finite element model, steel uses the isotropic elastoplastic model provided by ABAQUS software. This constitutive model complies with the Von Mises yield criterion and is commonly used to simulate the elastoplastic behavior of metal materials. A trilinear stress–strain relationship is used for steel, expressed as follows [26]:

$$\sigma_s = \begin{cases} E_s\varepsilon_s & \varepsilon_s \le \varepsilon_y \\ f_y & \varepsilon_y \le \varepsilon_s \le \varepsilon_{s,h} \\ f_y + E_{s,h}(\varepsilon_s - \varepsilon_{s,h}) & \varepsilon_{s,h} \le \varepsilon_s \end{cases}, \quad (5)$$

where σ_s is the stress of the steel, ε_s is the strain of steel, ε_y is the yield strain of steel, $\varepsilon_{s,h}$ is the strain corresponding to the onset of stress hardening, with a value of $\varepsilon_{s,h} = 10\varepsilon_y$, E_s is the elastic modulus of steel, and $E_{s,h}$ is the strength modulus of steel, with a value of $E_{s,h} = 0.01E_s$.

In Equation (5), the elastic modulus E_s is taken to be 2.06×10^5 MPa, the Poisson's ratio μ_c is 0.3 and f_y is 262.50 MPa. By substituting these into Equation (5), the stress–strain curve for the steel tube is obtained as shown in Figure 1c.

3. Experimental Data of T-Shaped CFST Short Columns Under Axial Compression

The experimental data for numerical analysis of the performance of T-shaped CFST short columns under axial compression using the finite element software ABAQUS were sourced from Chen et al. [27]. The cross-sectional form of the columns tested in Chen et al. [27] is shown in Figure 2.

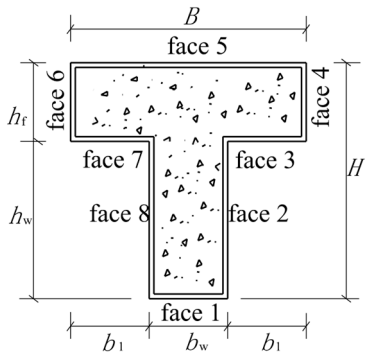


Figure 2. Section form of the column specimens [23].

The steel tube of the T-shaped CFST short column was composed of two bent plates and one straight plate welded together. The flange width B was equal to the total height H in the web direction, while parameters b_w and b_1 represent the width of the column web and the extension length of the column flange, respectively.

When the height of the specimen was within the range of 3 to 4 times the side length, the effect of the slenderness ratio on the axial compression behavior of the concrete-filled steel tube (CFST) column was negligible [26]. Accordingly, a length of L = 900 mm was designed to conform to this scenario. The compressive strength of the concrete cube (f_{cu}) was 38.22 MPa, and the elastic modulus of the concrete E_c was 2.924 × 10^4 MPa. The b_w and h_f of all specimens were 100 mm. The geometric dimensions, material properties, and related parameters of the specimens [27] and the T-shaped CFST short columns with the proposed stiffening ribs are shown in Table 2.

Table 2. Dimensions, mechanical properties of materials, and related parameters.

Index	t (mm)	$b_s \times b_h$ (mm)	b_t (mm)	f_y (MPa)	ζ	α
1-T300-6	6	—	—	262.50	1.615	0.017
2-T300-8	8	—	—	301.99	2.461	0.016
2-T300-8-(2)	8	—	—	262.50	2.139	0.015
3-T300-5	5	—	—	304.50	1.567	0.002
3-T300-5-(2)	5	—	—	262.50	1.351	0.004
4-T300-6J-A	6	25 × 25	6	262.50	1.831	0.020
5-T300-8J	8	25 × 25	8	262.50	2.416	0.020
6-T300-5J	5	25 × 25	5	262.50	1.534	0.021
7-T300-6J	6	20 × 20	6	262.50	1.783	0.021
8-T300-6J	6	30 × 30	6	262.50	1.879	0.020
9-T300-6J	6	35 × 35	6	262.50	1.927	0.019
10-T300-6J	6	25 × 25	6	335.00	2.337	0.022
11-T300-6J	6	25 × 25	6	345.00	2.407	0.023
12-T300-6J	6	25 × 25	6	390.00	2.720	0.024
13-T300-6J-B	6	25 × 25	6	262.50	1.831	0.019
14-T300-6J-C	6	25 × 25	6	262.50	1.831	0.023
15-T300-6J-D	6	25 × 25	6	262.50	1.831	0.022

Note: 1. For all specimens in the table, flange width B = 300 mm, and web height h_w = 200 mm. 2. Taking specimen 4-T300-6J-A as an example, 4 is the specimen number, T300-6J indicates a T-shaped web with a total height of 300 mm and a steel tube thickness of 6 mm, J signifies the presence of stiffening ribs, A denotes the cross-sectional form, t is the wall thickness of the steel tube, b_s is the length of the stiffening rib, b_h is the height of the stiffening rib, b_t is the thickness of the stiffening rib, f_y is the yield strength of the steel, ζ is the concrete confinement effect coefficient, and α is the concrete enhancement factor.

4. Finite Element Model of the CFST Short Columns

To prevent local damage due to stress concentration at both ends of the T-shaped CFST short columns during axial compression, rigid plates with a thickness of 25 mm were placed at both the bottom and top of the T-shaped CFST short columns when the finite element model was established. Both the rigid plates and the concrete were modeled using three-dimensional solid elements with reduced integration (also known as C3D8R in ABAQUS). Compared to other higher-order iso-parametric elements, the C3D8R elements have slightly lower computational accuracy. However, they significantly reduce the number of degrees of freedom and thus greatly save on computational time. The steel tube was modeled using shell elements with full integration (also known as S4R in ABAQUS). S4R elements belong to the finite strain shell elements and are suitable for large strain analysis. Shear deformation is allowed along the thickness direction. Depending on the shell thickness, the solution method will automatically conform to either thick shell theory or thin shell theory. When the shell thickness is very small, the shear deformation is minimal, and the finite membrane strain and large rotations are considered. To satisfy accuracy and facilitate convergence, the S4R elements used Simpson integration with nine integration points through the element thickness.

In actual projects, loads were consistently applied to both the steel elements and the core concrete through a series of measures, such as reasonable structural layout, correct construction techniques, ensuring the adhesion between the steel tube and concrete, and maintaining high-quality construction standards. When meshing the specimen, structured meshing technology was used for the rigid plates, concrete, and steel tube, with a mesh size of 25 mm. To avoid the influence of end plate bending on the simulation results during

loading, the upper and lower end plates were coupled to the centroid reference points RP-1 and RP-2, respectively. The rigid plates and concrete end face were constrained with a tie, while the rigid plates and the steel tube end face were constrained with a shell-to-solid coupling to ensure consistent rotation and displacement of the contact elements between the rigid plates, steel tube, and concrete. The generated mesh of the finite element model is shown in Figure 3.

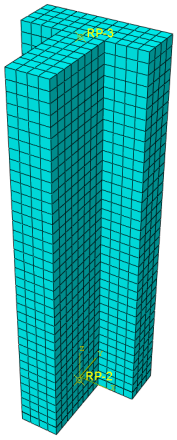


Figure 3. Mesh generation.

When the T-shaped CFST short column is close to failure, the deformation of the steel tube and concrete under axial load no longer remains consistent. Therefore, a Coulomb friction model was used to describe the behavior between them. The contact between the steel tube wall and the concrete surface consisted of tangential sliding and normal contact. Along the tangential direction of the contact surface, finite sliding with a Coulomb friction coefficient of 0.25 was used, while along the normal direction of the contact surface, hard contact was used. This allowed the steel tube and concrete to separate but not penetrate each other. This approach better simulated the actual interface performance.

The analysis and computation were conducted using the ABAQUS/Standard module. The following settings were adopted for the analysis: time period = 0.1, Nlgeom = off, maximum number of increments = 1×10^5, initial increment = 0.001, minimum increment = 1.0×10^{-12}, and maximum increment = 0.1. To facilitate model convergence, displacement loading was used. A fully fixed constraint was applied at reference point RP-2 at the base of the column. At reference point RP-1 at the top of the column, only a vertical displacement was applied.

Chen et al. [27] conducted an axial compression test on a T-shaped CFST short column specimen, 1-T300-6. The primary failure mode of the T-shaped CFST short column was local buckling under compression, with the overall column resembling a waist drum shape and the concrete in the concave corners being crushed. The test results indicated that the steel plate and concrete at the concave corners separated, and the steel plate at the concave corners did not provide any confining effect on the concrete. To numerically simulate the experimental testing by Chen et al. [27], a finite element analysis was performed on specimen 1-T300-6. The Von Mises stress contour plot is shown in Figure 4. The finite element analysis results mainly showed a buckling failure of the steel tube under compression. The concrete at the buckling locations and the concave corner areas also failed under compression. As the displacement increased, two buckling waves formed on face 5 of the steel tube, and outward buckling occurred at the middle concave corners. A comparative analysis of the results from the finite element analysis and the experimental test in Chen et al. [27] revealed consistent deformation characteristics at failure for both.

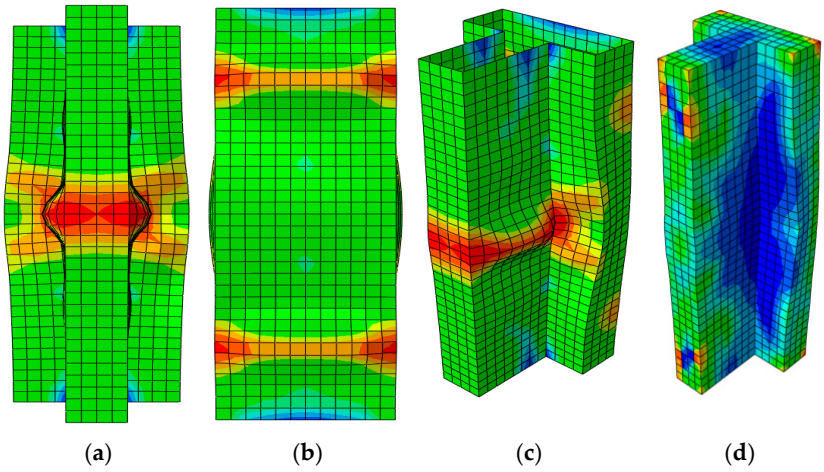


Figure 4. Stress contour plots of specimen 1-T300-6: (**a**) Shape of the overall column; (**b**) Face 5 buckling; (**c**) outward buckling at concave corners; (**d**) concrete at face 5.

To verify the accuracy of the finite element model, further analyses were conducted on specimens 1-T300-6, 3-T300-8, and 3-T300-5. The corresponding load–longitudinal displacement curves are plotted in Figure 5.

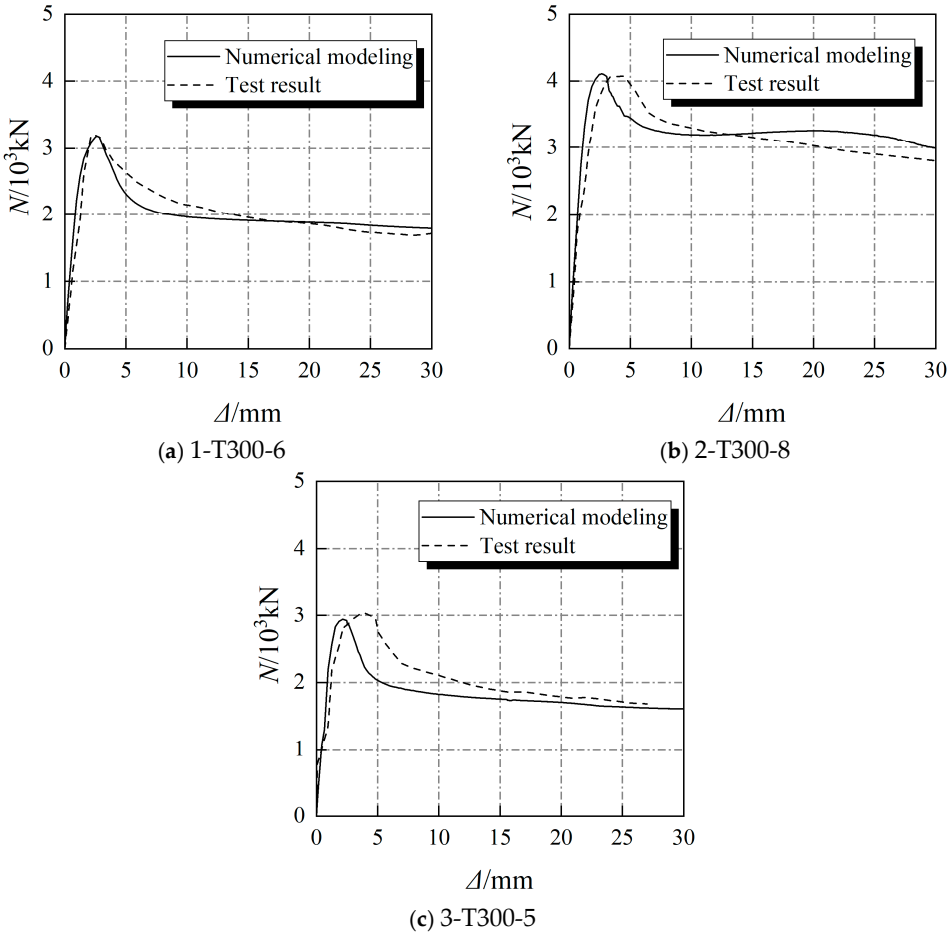


Figure 5. Comparison of load–longitudinal displacement curves from experimental tests and finite element simulations.

From the comparison between the curves from the finite element analysis (FEA) and the experimental tests, it can be observed that the stiffness in the ascending part of the load–longitudinal displacement curve obtained from the FEA was slightly higher than the

stiffness measured during the experimental test. This is because the FEA did not account for the residual stress caused by the welds connecting the steel tubes, which reduces the stiffness of the cross-section. Compared to the load–longitudinal displacement curve obtained from the experiment, the descending part of the curve from the FEA is smoother. This is because the FEA values do not consider the geometric nonlinearity effects of the steel tubes. The ultimate load-bearing capacity calculated via the FEA was slightly higher than that from the experimental test, as the FEA assumes a more uniform bond between the concrete and the steel tube compared with the experimental test. The ultimate load-bearing capacities obtained from both the FEA and the experiments are listed in Table 3.

Table 3. Comparison of ultimate bearing capacity between experimental tests and finite element simulations.

Index	N_e (10^3 kN)	N_u (10^3 kN)	N_u/N_e
1-T300-6	3.170	3.199	1.01
2-T300-8	4.077	4.147	1.02
3-T300-5	3.139	2.970	0.95

Note: N_e is the ultimate bearing capacity obtained from the experiments; N_u is the ultimate bearing capacity calculated from the finite element analysis.

Although there are certain differences in the stiffness of the ascending and descending parts of the load–longitudinal displacement curve obtained from the FEA compared to the experimental results, the simulation results were overall in good agreement with the experimental ones. The average ratio of the experimental value N_e to the calculated value N_u from the FEA is 0.99, with a standard deviation of 0.031. This is within the allowable error range in engineering practice.

By comparing the failure modes, characteristics of load–longitudinal displacement curves, and ultimate bearing capacities obtained from both the experiments and the finite element analyses, it can be concluded that the established finite element model can adequately simulate the performance of T-shaped CFST short columns under axial compression.

5. Comparison of Results from FEA Simulation of T-Shaped CFST Columns with and Without Stiffening Ribs

Taking specimen 1-T300-6 as an example, stiffening ribs can be added in different arrangements. The cross-sectional forms of the new T-shaped CFST column with stiffening ribs are shown in Figure 6.

According to the validated finite element model based on the above experiments, and taking specimen 4-T300-6J-A as an example, a comparison was made between the finite element simulation results with and without additional stiffeners. Figure 7 shows the stress contour maps of the finite element model for specimen 4-T300-6J-A.

By comparing Figure 4a,c and Figure 7a,c, it is evident that, when the specimen without stiffening ribs failed, the steel tube at the concave corners of the specimen provided weak confinement to the core concrete. Stress concentration first occurred on faces 2 and 3 of the specimens; with an increase in the load, the stress gradually dispersed in all directions. A transverse bulging wave formed in the middle of the specimen, resulting in a waist drum shape. Ultimately, bulging failure occurred at the concave corners. For specimen 4-T300-6J-A, the addition of stiffening ribs enhanced the confinement of the core concrete by the steel tube. As the load increased, the high-stress range at the concave corners was relatively small, mainly concentrated at the concave corners in the middle of the specimen. Three transverse bulging waves formed in the middle of the steel tube. This indicates that adding stiffening ribs can effectively reduce the degree of stress concentration in the specimen under axial loads.

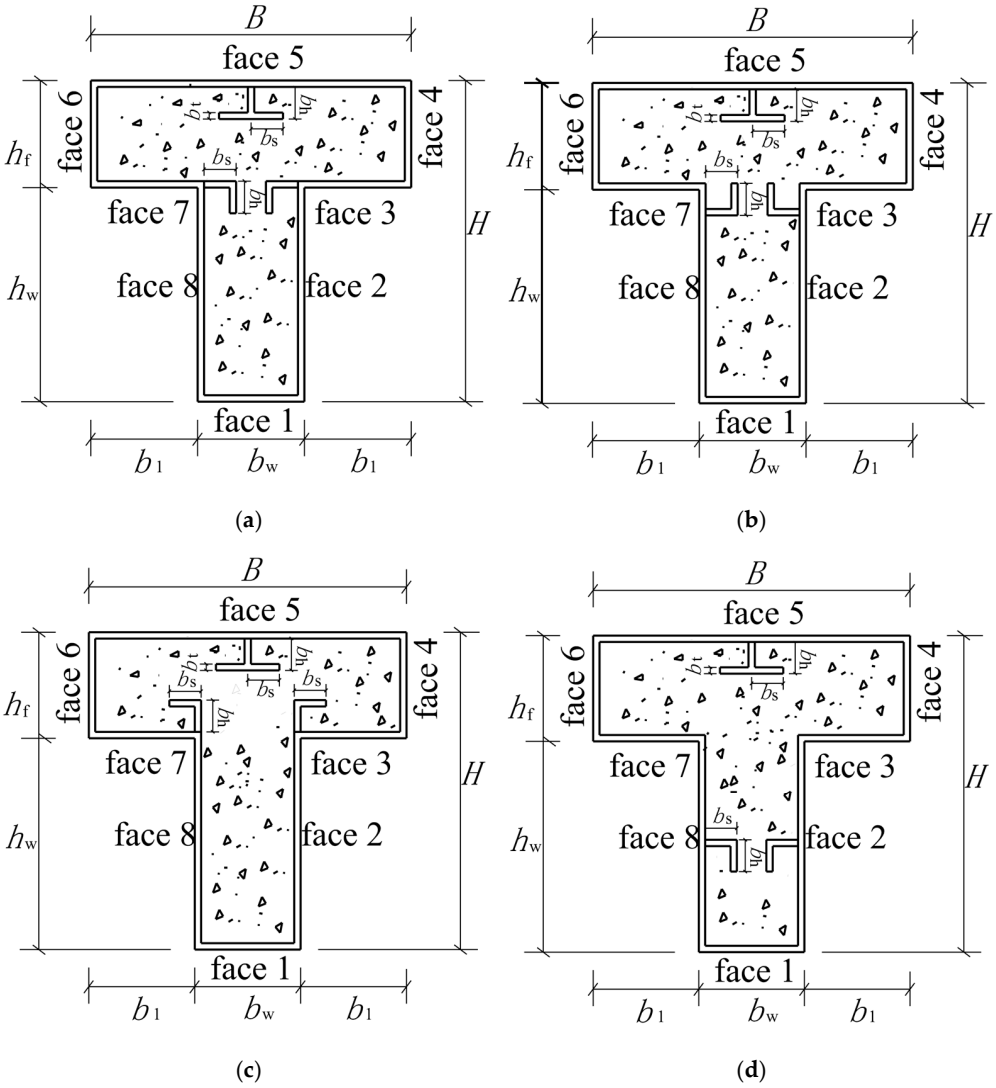


Figure 6. Different arrangements of stiffening ribs on T-shaped concrete-filled steel tube short columns: (**a**) The first type of stiffening ribs' arrangement; (**b**) The second type of stiffening ribs' arrangement; (**c**) The third type of stiffening ribs' arrangement; (**d**) The fourth type of stiffening ribs' arrangement.

When comparing Figure 4b,d and Figure 7b,d, it is clear that when the specimen without stiffening ribs failed, there were two noticeable bulging waves on face 5, and significant buckling was observed in the steel tube. The overall specimen showed bulging behavior. In contrast, for the specimen with stiffening ribs, due to the constraining effect, only slight bulging occurred in the middle of face 5, and the overall bending degree of the specimen was relatively small. This indicates that adding stiffening ribs can effectively delay the local outward buckling of the steel tube, improve the overall stability of the steel tube, and enhance the constraining effect of the steel tube on the concrete.

Figure 8 compares the load–displacement curves of T-shaped CFST short columns with and without stiffening ribs. Figure 8 shows that, with the use of the new stiffeners, the descending part of the load–displacement curve of the T-shaped CFST short column became smoother.

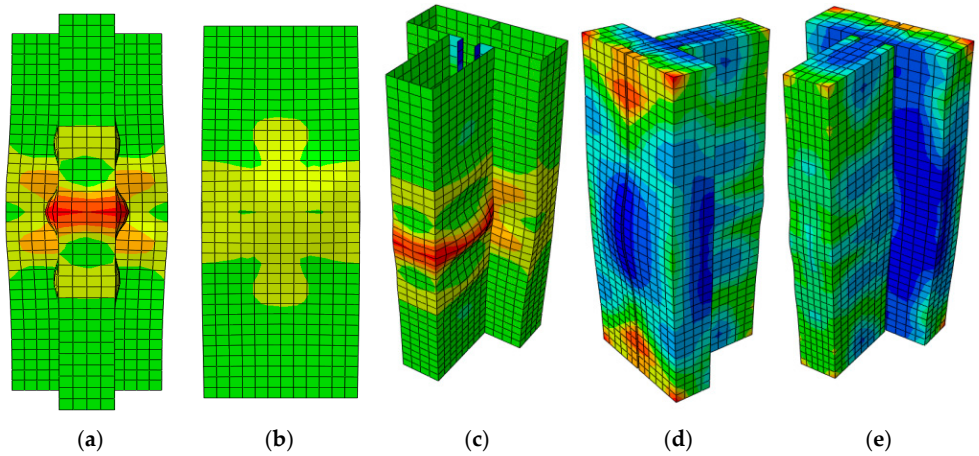


Figure 7. Stress contour plots of specimen 4-T300-6J-A: (**a**) Shape of the overall column; (**b**) Face 5 buckling; (**c**) outward buckling at concave corners; (**d**) concrete at face 5; (**e**) concrete at concave corners.

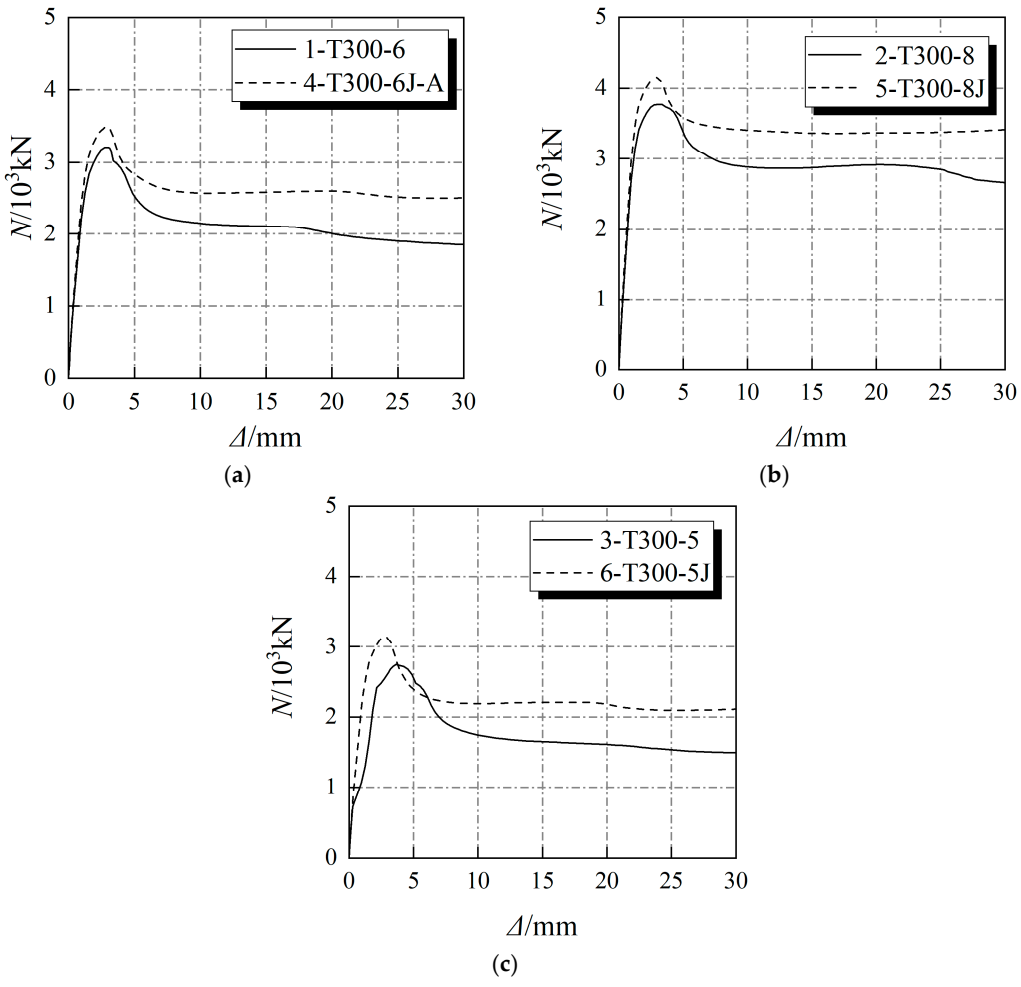


Figure 8. Comparison of load–longitudinal displacement curves of T-shaped CFST short columns with and without stiffening ribs under axial compression: (**a**) The wall thickness of the steel tube is 6 mm; (**b**) The wall thickness of the steel tube is 6 mm; (**c**) The wall thickness of the steel tube is 5 mm.

Table 4 compares the ultimate bearing capacities of T-shaped CFST short columns with and without stiffening ribs using finite element simulations. From Table 4, it is evident that the proposed stiffening ribs can significantly increase the ultimate bearing capacities of T-shaped CFST columns. Comparing specimen 1 with 4, specimen 2 with 5, and specimen

3 with 6, we found that the ultimate bearing capacities increased by 9.87%, 10.00%, and 9.60%, respectively.

Table 4. Comparison of ultimate bearing capacities of T-shaped CFST short columns with and without stiffening ribs under axial compression.

Index	$b_t \times b_h$ (mm)	b_t (mm)	S_r (mm^2)	N_u (10^3 kN)
1-T300-6	—	—	0	3.199
2-T300-8-(2)	—	—	0	3.772
3-T300-5-(2)	—	—	0	2.746
4-T300-6J-A	25 × 25	6	642	3.478
5-T300-8J	25 × 25	8	808	4.147
6-T300-5J	25 × 25	5	550	3.147

Note: b_t and S_r are the thickness and the total area of the stiffening ribs, respectively.

6. Effects of Key Parameters on Axial Loading Capacity of the T-Shaped CFST Columns

Parametric studies were conducted to evaluate the effects of key parameters on the axial loading capacity and ductility of the T-shaped CFST columns.

Using the specimen 4-T300-6J-A as a reference, we analyzed the effects of the thickness, specifications, strength, and arrangement of stiffening ribs on the axial compressive behavior of T-shaped CFST short columns. Table 5 presents the ultimate bearing capacities obtained from the finite element analyses of the T-shaped CFST short columns with stiffening ribs.

Table 5. Ultimate bearing capacities of T-shaped CFST short columns with stiffening ribs.

Group ID	Index	N_u (10^3 kN)	Index to Be Compared	Percentage Increase
A	4-T300-6J-A	3.478	6-T300-5J	10.51%
	5-T300-8J	4.147	6-T300-5J	31.77%
	6-T300-5J	3.147	6-T300-5J	0%
B	4-T300-6J-A	3.478	7-T300-6J	1.25%
	7-T300-6J	3.435	7-T300-6J	0%
	8-T300-6J	3.527	7-T300-6J	2.67%
	9-T300-6J	3.578	7-T300-6J	4.16%
C	4-T300-6J-A	3.478	4-T300-6J-A	0%
	10-T300-6J	4.082	4-T300-6J-A	17.36%
	11-T300-6J	4.166	4-T300-6J-A	19.78%
	12-T300-6J	4.539	4-T300-6J-A	30.50%
D	4-T300-6J-A	3.478	4-T300-6J-A	0%
	13-T300-6J-B	3.465	4-T300-6J-A	−0.37%
	14-T300-6J-C	3.505	4-T300-6J-A	0.77%
	15-T300-6J-D	3.494	4-T300-6J-A	0.46%

By comparing the ultimate bearing capacities of the specimens each group in Table 5, the following conclusions can be drawn:

(1) Increasing the thickness of the stiffening ribs significantly improved the bearing capacities of the specimens. When the thickness of the stiffening ribs increased from 5 mm to 8 mm, the ultimate bearing capacity increased by 10.51% to 31.77% accordingly.

(2) Changes in the specifications of the angle steel had an insignificant effect on the ultimate bearing capacities of the specimens, with the variation in ultimate bearing capacity being within 5%.

(3) The strength of the stiffening rib material significantly enhanced the load-bearing capacities of the specimens. When the steel strength increased from 262.50 MPa to 345 MPa and 390 MPa, the ultimate bearing capacity increased by 17.36%, 19.78%, and 30.50% respectively.

(4) Changes in the arrangement of the stiffening ribs had an insignificant effect on the ultimate bearing capacities of the specimens, with the variation in ultimate bearing capacity being within ±1%.

Effects of Key Parameters on Ductility of the T-Shaped CFST Columns

Ductility reflects the ability of structural components to undergo deformation at later stages and absorb energy. It is crucial for ensuring the overall load-bearing capacity of the structure and exploiting its redundancy potential. Additionally, it helps prevent progressive collapse of the structure. Ductility is represented by the ductility coefficient, which is expressed as follows [28,29]:

$$D_{\mathrm{I}} = \Delta_{\mathrm{u}} / \Delta_{\mathrm{y}} \tag{6}$$

where Δ_{u} is the axial displacement when the load drops to 85% of the peak load and Δ_{y} is the displacement corresponding to the yield point on the load–displacement curve, determined by the energy method.

Figure 9 shows the load–longitudinal displacement curves of the T-shaped CFST short columns under axial compression using finite element analyses. The ductility coefficients obtained from Equation (6) are listed in Table 6.

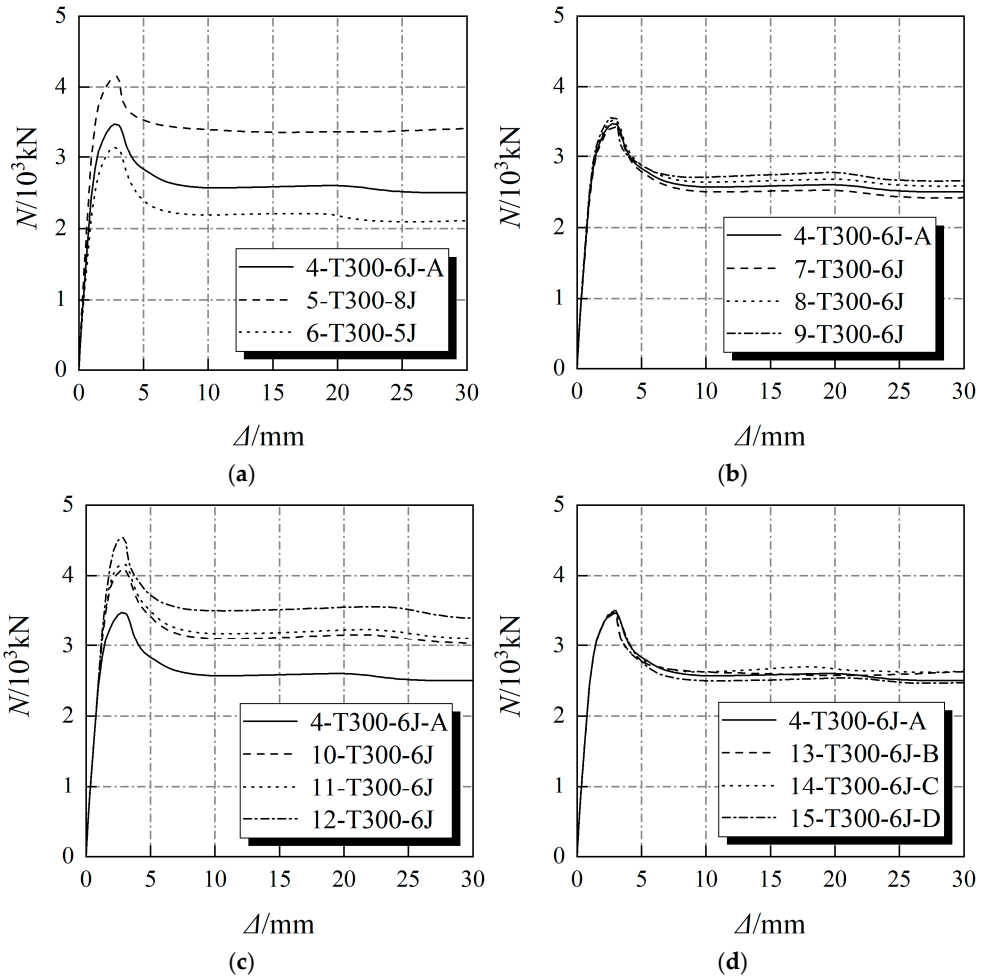


Figure 9. Load–longitudinal displacement curves of the T-shaped CFST short columns with stiffening ribs: (**a**) thickness of stiffening ribs; (**b**) specifications of stiffening ribs; (**c**) strength of stiffening ribs; (**d**) arrangements of stiffening ribs.

According to the ductility coefficients in Table 6, the ductility coefficient histogram is plotted as shown in Figure 10.

Table 6. Ductility coefficients of the T-shaped CFST short columns with stiffening ribs.

Group ID	Index	N_u (10^3 kN)	Index to Be Compared	Percentage Increase
A	4-T300-6J-A	8.850	6-T300-5J	6.48%
	5-T300-8J	9.741	6-T300-5J	17.20%
	6-T300-5J	8.311	6-T300-5J	0%
B	4-T300-6J-A	8.850	7-T300-6J	5.11%
	7-T300-6J	8.419	7-T300-6J	0%
	8-T300-6J	9.138	7-T300-6J	8.54%
	9-T300-6J	9.097	7-T300-6J	8.05%
C	4-T300-6J-A	8.850	4-T300-6J-A	0%
	10-T300-6J	9.912	4-T300-6J-A	12%
	11-T300-6J	10.078	4-T300-6J-A	13.87%
	12-T300-6J	10.967	4-T300-6J-A	23.92%
D	4-T300-6J-A	8.850	4-T300-6J-A	0%
	13-T300-6J-B	9.133	4-T300-6J-A	3.19%
	14-T300-6J-C	9.242	4-T300-6J-A	4.42%
	15-T300-6J-D	8.722	4-T300-6J-A	−1.44%

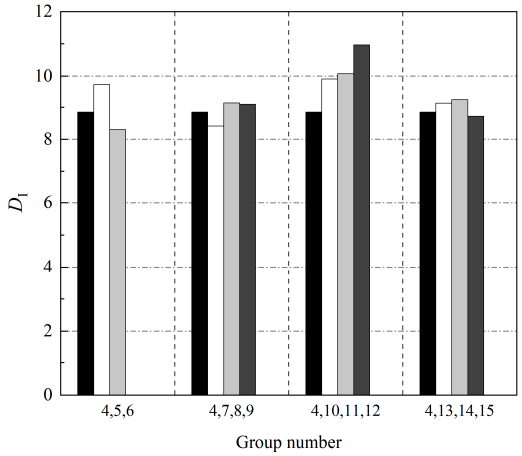


Figure 10. Ductility coefficient histogram.

Based on a comparison of Figures 9 and 10 and Table 6, we can draw the following inferences:

(1) With an increase in the thickness of stiffening ribs, the ductility coefficients of the specimens gradually increased. When the thickness of the stiffening ribs increased from 5 mm to 8 mm, the ductility coefficient improved by 17.20%. The main reasons for this are that an increase in the thickness of the stiffening ribs enhances the transverse stiffness of the steel tube, delays local buckling of the steel tube, and strengthens the confinement effect on the core concrete.

(2) The change in the specifications of the stiffening ribs had a significant effect on the ductility of the specimens. When the specifications changed from 20 mm × 20 mm to 30 mm × 30 mm, the ductility coefficient increased by 8.54%. Further increasing the size to 35 mm × 35 mm resulted in a reduced rate of increase in the ductility coefficient. The main reason for this is that, when the specifications of the stiffening ribs are too large, the overall stiffness of the specimens increases significantly, while the change in the increase of the transverse stiffness of the steel tube is not substantial. Thus, it only has a limited impact on the overall deformation capacity of the specimens.

(3) As the strength of the stiffening rib material increased, the ductility coefficient of the specimens increased significantly. When the steel strength increased from 262.50 MPa to 390 MPa, the ductility coefficient improved by 12% to 23.92%. The main reason for this is that, similar to increasing the thickness of the stiffening ribs, enhancing the strength of the stiffening ribs can significantly improve the transverse stiffness of the steel tube, suppress

local buckling of the steel tube, and consequently enhance the confinement effect on the core concrete.

(4) The change in the arrangements of the stiffening ribs had an insignificant effect on the ductility of the specimens. In arrangement type c shown in Figure 6, the ductility coefficient only increased by 4.42%, while in arrangement type d, the ductility coefficient decreased by 1.44%. The main reason for this is that the change in the arrangement form of the stiffening ribs may only cause local changes in stiffness in specific areas, whereas the overall stiffness of the structure does not change significantly. The overall stiffness of the specimen mainly depends on material properties and overall geometric dimensions, and the change in the arrangement form of the stiffening ribs has a limited impact on the overall stiffness.

7. Conclusions

To improve the performance of T-shaped CFST columns, a new type of stiffening rib was proposed. A finite element model was established using the general-purpose commercial software ABAQUS. After the finite element model was validated by comparison with experimental results, parametric studies were conducted to examine the effect of key parameters on the load-bearing capacity and ductility of T-shaped CFST columns under axial compression. The main conclusions are as follows:

- As verified using experimental data, the developed finite element model can adequately simulate the failure modes, deformation characteristics, and ultimate bearing capacity of T-shaped CFST short columns.
- Compared with T-shaped CFST short columns without stiffening ribs, the new stiffening ribs can significantly reduce the degree of buckling deformation of the steel tube, improve the confining effect on the core concrete, and enhance the combined performance of the steel tube and the concrete.
- The ultimate bearing capacity of specimens can be significantly improved by increasing the thickness of stiffeners and the strength of materials. Changes in the specifications and arrangements of the stiffening ribs have little effect on the ultimate bearing capacity of the specimens, with changes in angle steel specifications causing variations within 5% and changes in arrangements causing variations within $\pm 1\%$.
- Increasing the thickness and material strength of the stiffening ribs significantly improves the ductility coefficients of the specimens. Enhancing the thickness and material strength of the stiffening ribs can delay local buckling of the steel tube and enhance the confinement effect on the core concrete. Changes in the specifications and arrangements of the stiffening ribs have little effect on the ductility of the specimens. When the angle steel specification increases from 20 mm $\times$ 20 mm to 30 mm $\times$ 30 mm, the ductility coefficient increases by only 8.54%, and when it further increases to 35 mm $\times$ 35 mm, the increase rate of the ductility coefficient decreases. The ductility coefficient of the c-type arrangement increases by only 4.42%, while the ductility coefficient of the d-type arrangement decreases by 1.44%.

Author Contributions: Conceptualization, X.Y.; methodology, X.Y. and G.F.; software, H.Y.; validation, H.Y.; formal analysis, G.F. and J.L.; investigation, X.Y.; resources, Y.S.; data curation, H.Y. and J.L.; writing—original draft preparation, H.Y., M.M.R. and J.L.; writing—review and editing, G.F.; visualization, M.M.R.; supervision, X.Y.; project administration, Y.S.; funding acquisition, Y.S. All authors have read and agreed to the published version of the manuscript.

Funding: This research was supported by the International Science and Technology Cooperation Program of Henan Province, Grant Number 241111521200, and the Natural Science Foundation of Henan Province, Grant Number 242300420063.

Data Availability Statement: The data that support the findings of this study are available from the corresponding author upon reasonable request.

Conflicts of Interest: The authors declare no conflict of interest.

References

1. Luo, R.K.; Shu, P.G.; Qin, Y. Performance of Concrete-filled Steel Tubular Stub Columns Reinforced with Annular Stiffener under Axial Compression: Experiment, simulation and design. *Structures* **2024**, *70*, 107903. [CrossRef]
2. Li, H.; Tao, Z.; Han, D. Finite Element Analysis of Axial Compression Behavior of L-Shaped Concrete-Filled Steel Tubular Columns with Different Combination. *Buildings* **2024**, *14*, 730. [CrossRef]
3. Liu, W. *Research on Mechanism of Concrete-filled Tubes Subjected to Local Compression*; Fuzhou University: Fuzhou, China, 2005.
4. Wang, Z.; Zhou, X.; Wei, F. Performance of Special-shaped Concrete-filled Square Steel Tube Column under Axial Compression. *Adv. Civil Eng.* **2020**, *2020*, 1763142. [CrossRef]
5. Yang, W.; Yang, Y.; Xu, W. Practical Temperature Calculation and Fire-resistant Design of Special-shaped Concrete-filled Steel Tubular Columns. *J. Constr. Steel Res.* **2023**, *210*, 10799237. [CrossRef]
6. Wang, D.; Lu, X. Experimental Study on Seismic Behavior of Concrete-filled Steel T-section and L-section Columns. *J. Build. Struct.* **2005**, *26*, 39–44+106.
7. Ilanthalir, A.; Regin, J.J.; Maheswaran, J. Concrete-filled Steel Tube Columns of Different Cross-sectional Shapes under Axial Compression. *Mater. Sci. Eng.* **2020**, *983*, 012007. [CrossRef]
8. Ye, Q.; Hao, F.; Xue, B. Review on Configurations of Concrete-filled Steel Tubular (CFST) Special-shaped Columns and Corresponding Beam-column Joint. *J. Beijing Univ. Technol.* **2021**, *47*, 1083–1094.
9. Ayough, P.; Ibrahim, Z.; Sulong, N.H.R. The Effects of Cross-sectional Shapes on the Axial Performance of Concrete-filled Steel Tube Columns. *J. Constr. Steel Res.* **2021**, *176*, 55–84. [CrossRef]
10. Cao, B.; Dai, S.; Huang, J. Experimental Study on Axial Compressive Behavior of Composite T-shaped Concrete-filled Steel Tubular Columns. *J. Build. Struct.* **2014**, *35*, 36–43.
11. Chen, X.; Zhou, T.; Chen, Z. Mechanical Properties of Special-shaped Concrete-filled Steel Tube Columns under Eccentric Compression. *J. Constr. Steel Res.* **2020**, *167*, 105779–105796. [CrossRef]
12. Zhao, J.; Zhao, H.; Zhang, C. Axial Compressive Bearing Capacity of Multi-cell T-shaped Concrete-filled Steel Tubular Column Based on Unified Strength Theory. *J. Guangxi Univ. (Nat. Sci. Ed.)* **2017**, *42*, 10–17.
13. Li, H.; Tong, Y.; Yin, J. Study on Axial Compression Behavior of Cross-shaped and L-shaped Multi-cavity Concrete-filled Steel Tube Special Shaped Column. *Int. J. Steel Struct.* **2022**, *22*, 153–175. [CrossRef]
14. Li, Q.; Zhou, X.; Li, G. Experimental Study on Behavior of Special T-shaped Composite Column with Compression Performance of Square Steel Tube Concrete Concrete-filled Square Steel Tubular under Eccentric Loads. *J. Civil Environ. Eng. (Chin. Engl.)* **2021**, *43*, 102–111.
15. Zhang, T.; Lyu, X.; Liu, H. Analysis of Finite Element Mechanism of Axial Compressive Behavior of T-Shaped Stiffened Concrete-Filled Steel Tubular Stub Columns After Uniform Fire Exposure. *Int. J. Steel Struct.* **2021**, *3*, 1–14. [CrossRef]
16. Cui, W.; Liu, S. Finite Element Analysis on Seismic Behavior of T-shaped Concrete-filled Steel Tube Columns with Double Nickelclad. *Build. Sci.* **2020**, *36*, 89–95.
17. Yin, F.; Xue, S.D.; Cao, W.L. Experimental and Analytical Study of Seismic Behavior of Special-shaped Multicell Composite Concrete-filled Steel Tube Columns. *J. Struct. Eng.* **2020**, *146*, 04019170. [CrossRef]
18. Zuo, Z.; Cai, J.; Qian, Q. Experimental Study on T-shaped CFT Stub Columns with Binding Bars Subjected to Axial Compression. *China Civil Eng. J.* **2011**, *44*, 43–51.
19. Zheng, Y.; Zeng, S. Flexural Behavior of Stiffened and Multi-cell T-shaped CFST Members with Different Loading Angles. *J. Build. Struct.* **2022**, *43*, 198–207+219.
20. Huang, H.; Zha, B.J.; Yang, C. Mechanical Behavior of T-shaped Concrete-filled Steel Ribbed Tubular Short Columns. *J. Build. Struct.* **2018**, *39*, 132–137.
21. Lu, Q.; Zhao, C.; Li, Y. Finite Element Analysis of Diagonal Honeycomb Stiffener T-shaped Concrete-filled Steel Tube Column under Earthquake. *Earthq. Resist. Eng. Retrofit.* **2022**, *44*, 42–48.
22. Alatshan, F.; Osman, S.A.; Hamid, R. Stiffened Concrete-filled Steel Tubes: A systematic review. *Thin-Walled Struct.* **2020**, *148*, 106590. [CrossRef]
23. Ma, T.F.; Chen, Z.H.; Khan, K. Experimental and Numerical Analysis of L-shaped Column Composed of Recycled Aggregate Concrete-Filled Square Steel Tubes under Eccentric Compression. *Adv. Steel Constr.* **2023**, *19*, 177–184.
24. Meng, B.; You, K.; Yang, B. Anti-progressive Collapse Performance and Design Method of Novel T-stub Connections. *Eng. Struct.* **2024**, *319*, 118880. [CrossRef]

25. Bao, M.; Hui, L.; Richard, J.L. Enhancing the Collapse Resistance of a Composite Subassembly with Fully Welded Joints Using Sliding Inner Cores. *J. Struct. Eng.* **2024**, *150*, 04024085.
26. Han, L. *Concrete Filled Steel Tubular Structures from Theory to Practice*, 4th ed.; Science Press: Beijing, China, 2022.
27. Chen, Y.; Shen, Z.; Lei, M. Experimental Investigation on Concrete-filled T-shaped Steel Tube Stubs Subjected to Axial Compression. *J. Tongji Univ. (Nat. Sci. Ed.)* **2016**, *44*, 822–829.
28. Feleb, M.; Fidelis, M. Stress Concentration Factors of Concrete-Filled T-Joints under In-Plane Bending: Experiments, FE Analysis and Formulae. *Materials* **2022**, *15*, 6421. [CrossRef] [PubMed]
29. Yin, X. Evaluation and Determination Methods on Yield Point of Structural Components Without Obvious Yield Feature. *Earthq. Eng. Eng.* **2019**, *39*, 143–150.

Disclaimer/Publisher's Note: The statements, opinions and data contained in all publications are solely those of the individual author(s) and contributor(s) and not of MDPI and/or the editor(s). MDPI and/or the editor(s) disclaim responsibility for any injury to people or property resulting from any ideas, methods, instructions or products referred to in the content.